molecules

MDPI

Article

Preparation, Characterization, and Electrochemical Performance of the Hematite/Oxidized Multi-Walled Carbon Nanotubes Nanocomposite

Hadeel M. Banbela [1,2], Laila M. Alharbi [1], Reema H. Al-Dahiri [3], Mariusz Jaremko [4] and Mohamed Abdel Salam [1,*]

[1] Department of Chemistry, Faculty of Science, King Abdulaziz University, P.O. Box 80200, Jeddah 21589, Saudi Arabia; hbanbela@stu.kau.edu.sa (H.M.B.); lalhrbi@kau.edu.sa (L.M.A.)
[2] Department of Chemistry, College of Science and Arts at Khulis, University of Jeddah, P.O. Box 355, Jeddah 21959, Saudi Arabia
[3] Department of Chemistry, College of Science, University of Jeddah, P.O. Box 34, Jeddah 21959, Saudi Arabia; rhal-dhahery@uj.edu.sa
[4] Smart-Health Initiative (SHI), Red Sea Research Center (RSRC), Biological and Environmental Science and Engineering (BESE) Division, King Abdullah University of Science and Technology (KAUST), P.O. Box 4700, Thuwal 23955-6900, Saudi Arabia; mariusz.jaremko@kaust.edu.sa
* Correspondence: masalam16@hotmail.com; Tel.: +966-541886660; Fax: +966-2-6952292

Abstract: In this research work, a hematite (α-Fe_2O_3) nanoparticle was prepared and then mixed with oxidized multi-walled carbon nanotubes (O-MWCNT) to form a stable suspension of an α-Fe_2O_3/O-MWCNTs nanocomposite. Different characterization techniques were used to explore the chemical and physical properties of the α-Fe_2O_3/O-MWCNTs nanocomposite, including XRD, FT-IR, UV-Vis, and SEM. The results revealed the successful formation of the α-Fe_2O_3 nanoparticles, and the oxidation of the MWCNT, as well as the formation of stable α-Fe_2O_3/O-MWCNTs nanocomposite. The electrochemical behaviour of the α-Fe_2O_3/O-MWCNTs nanocomposite was investigated using cyclic voltammetry (CV) and linear sweep voltammetry (LSV), and the results revealed that modification of α-Fe_2O_3 nanoparticles with O-MWCNTs greatly enhanced electrochemical performance and capacitive behaviour, as well as cycling stability.

Keywords: hematite; nanoparticle; MWCNT; electrochemical performance; capacitive behaviour

Citation: Banbela, H.M.; Alharbi, L.M.; Al-Dahiri, R.H.; Jaremko, M.; Abdel Salam, M. Preparation, Characterization, and Electrochemical Performance of the Hematite/Oxidized Multi-Walled Carbon Nanotubes Nanocomposite. *Molecules* **2022**, *27*, 2708. https://doi.org/10.3390/molecules27092708

Academic Editors: Hassan Hasan Hammud and Nadeem S. Sheikh

Received: 20 February 2022
Accepted: 19 April 2022
Published: 22 April 2022

1. Introduction

Nanotechnology is a general term focused on the manipulation and applications of nanoparticles (NPs), such as metals, metal oxides, semiconductors, ceramics, and polymers, due to their outstanding structural, physicochemical and morphological properties, which allows them to be used in a wide variety of applications, especially in the energy sector. For example, many metal oxides are used as electrodes for lithium-ion batteries (LIBs) due to their outstanding and efficient surface area, as well as for their chemical suitability and stability, as they intercalate/deintercalate lithium ions into their layered structure [1–3], which significantly enhances LIB storage capacities even beyond their theoretical values [4]. Hematite (α-Fe_2O_3) nanostructures are one of the promising metal oxide nanoparticles which have attracted the attention of researchers and are used for a variety of applications, including splitting of water and the production of hydrogen gas [5], magnetic storage devices [6], potential gas sensors [7], targeted drug delivery [8], and biomedical applications [9], as well as LIB production [10–13].

Oxygen evolution reaction (OER) has become the common power source for sustainable energy development technology, especially the photoelectrochemical (PEC) cells, which use solid-state electrodes in a similar way to conventional electrolysers such as in oxygen evolution reactions (OER, oxidation) and hydrogen evolution reactions (HER,

reduction), which take place at two different solid/liquid junctions. In PEC cells, at least one of the electrodes consists of a semiconductor capable of absorbing the incoming light, in which a depletion (or space-charge, SC) region is formed at equilibrium, and the photogenerated charges are separated by the electric field in the SC region and travel to a solid/liquid junction where they take part in either the HER or the OER. The electro-catalysts of non-noble metals have been interesting in this field; reportedly, Hematite has an outstanding performance of oxygen evolution reaction (OER), with an optical narrow bandgap around ~2.2 eV, which absorbs light up to 560 nm and which allows it to absorb 40% of solar irradiance. Hematite is a naturally abundant, low-cost material, and has good chemical stability in aqueous solutions in a broad pH range. The position of the valence band is suitable for oxygen evolution, which makes it an ideal candidate photoanode material for solar water splitting [14,15]. Conversely, hematite has shown low efficiency because of its poor electrical conductivity. The critical reasons are high recombination of electrons and holes, low mobility of the holes/short holes diffusion length and trapping of electrons by oxygen deficiency sites. Various techniques are reported in the literature to improve the efficiency of hematite by inserting the effective materials in the lattice without disturbing the structure of the crystal. Enhancing the efficiency of hematite for photoelectrochemical water splitting was carried out by doping with elements/ions such as Ti^{4+} [16], manganese [17], zirconium and tin [18], tantalum [19], boron [20], phosphorous [21], rhodium [22], and tetravalent dopants (Si^{4+}, Sn^{4+}, Ti^{4+}, and Zr^{4+}) [23]. Few works have been dedicated to doping with carbon-based materials such as carbon dots [24,25] and graphene [26,27]. Although, one of the computational studies showed that the water splitting of hematite could be significantly improved by forming composites with carbon nanotubes [28]; the number of studies focusing on this topic is scarce in the literature [29].

In this work, the electrochemical behaviour of the hematite/oxidized multi-walled carbon nanotubes (O-MWCNT) nanocomposite was studied and explored. First, hematite was prepared using the hydrothermal method and was then mixed with the oxidized MWCNTs to form a stable nanocomposite. The hematite/O-MWCNTs nanocomposite was then characterized by XRD in order to explore the chemical and physical characteristics. The electrochemical behaviour of the O-MWCNT/hematite nanocomposite were investigated using cyclic voltammetry (CV) and linear sweep voltammetry (LSV) to explore their possible applications.

2. Experimental

2.1. Chemicals and Materials

Ferric chloride hexahydrate ($FeCl_3 \cdot 6H_2O$) was obtained from Lobachemie and was used as received without further purification. Multi-walled carbon nanotubes (MWCNT) were provided from Sigma-Aldrich (St. Louis, MI, USA). Sulfuric acid—95–99% (H_2SO_4) and nitric acid—65% (HNO_3) were purchased from Chem-Lab. (Bunkyo, Tokyo). Potassium hydroxide (KOH) was obtained from Fluka Chemie AG (Buchs, Switzerland). All aqueous solutions were prepared with distilled water.

2.2. Preparation of Hematite (α-Fe_2O_3) Nanoparticles

The hematite nanoparticles were prepared according to the procedure used by Faust et al. [30]. Initially, 30 mL solution of 0.1 M $FeCl_3 \cdot 6H_2O$ was dissolved in distilled water and added dropwise into 120 mL stirred boiling water; subsequently, the solution was refluxed for 5 min and finally cooled in an ice bath. The colloidal α-Fe_2O_3 suspension had a dark red colour and was acidic:

$$2\ FeCl_3 + 3\ H_2O \rightarrow \alpha\text{-}Fe_2O_3 + 6\ HCl$$

The colloid was dialyzed by using a dialysis tube (Medicell International, MWCO 12,000–14,000) in the distilled water, which changed several times until the pH had reached pH~6 and the electrical conductivity was below 20 S cm^{-1}. The product was kept in the dark.

2.3. Oxidation of MWCNT

The purification and oxidation of MWCNTs were performed as follows: 1.0 g of the pristine MWCNTs was added to 200 mL solution of concentrated HNO_3/H_2SO_4 (1:3; v/v) in an ice bath. The mixture was sonicated for 4 h in an ultrasonic bath at 40 °C. The resulting solution was then transferred to a 1000 mL beaker with distilled water to reduce the acidity of the product, which was then neutralized by using a dialysis tube (Medicell International, MWCO 12,000–14,000) in the distilled water, that were changed several times until achieving a neutral pH.

2.4. Preparation of α-Fe_2O_3/O-MWCNTs Nanocomposite

The hematite was deposited onto the surface of MWCNTs by mixing at RT for one hour under ultrasonication with different concentrations of MWCNT.

All prepared suspensions before and after mixing were dried overnight in an oven at 50 °C. For further characterisation, the solutions and the powder were obtained in the dark.

For XRD measurements, the resulting powder was calcined at 200 °C for 2 h at a heating rate of 5 °C min^{-1} in a preheated muffle furnace.

2.5. Electrode Fabrication

The α-Fe_2O_3 and α-Fe_2O_3/O-MWCNTs electrodes were prepared for electrochemical investigations. Approximately 50 µL of the prepared suspensions was dropcasted upon the glassy carbon electrode (GCE) in a rotating ring disk electrode system (RRDE), which was used as a working electrode.

2.6. Characterization

The optical absorptions of the prepared hematite with different pH values were investigated by using a MultiSpec-1501 UV–Vis Spectrophotometer (SHIMADZU). The determination of the functional group on the surface of the MWCNTs was performed with a PerkinElmer Spectrum 100 infrared spectrometer (FTIR spectra), where the dried samples were mixed with potassium bromide (ratio of 1:10) and pressurized to produce KBr pellet for FTIR measurements. The identification of crystalline phases of the samples was recorded using a Bruker D2 Phaser X-ray diffractometer. The XRD measurements were carried out by CuKα radiation (1.5418 Å). The XPS experiments were performed on a Kratos Axis Ultra DLD instrument equipped with a monochromatic Al Kα X-ray source (hν = 1486.6 eV) operating at a power of 75 W and under UHV conditions in the range of $\sim 10^{-9}$ mbar. All spectra were recorded in hybrid mode using electrostatic and magnetic lenses and an aperture slot of 300 × 700 µm. The survey and high-resolution spectra were acquired at fixed analyser pass energies of 160 and 20 eV, respectively. The samples were mounted in floating mode in order to avoid differential charging. Thereafter, XPS spectra were acquired using charge neutralization. The XPS experiments were performed on a Kratos Axis Ultra DLD instrument equipped with a monochromatic Al Kα X-ray source (hν = 1486.6 eV) operating at a power of 75 W and under UHV conditions in the range of $\sim 10^{-9}$ mbar. All spectra were recorded in hybrid mode using electrostatic and magnetic lenses and an aperture slot of 300 × 700 µm. The survey and high-resolution spectra were acquired at fixed analyser pass energies of 160 and 20 eV, respectively. The samples were mounted in floating mode in order to avoid differential charging. Thereafter, XPS spectra were acquired using charge neutralization.

2.7. Electrochemical Measurements

The electrochemical measurements included cyclic voltammetry (CV) and linear sweep voltammetry (LSV), and the electrochemical impedance spectroscopy (EIS) studies were performed using the CorrTest electrochemical workstation with an RRDE three-electrode system. The working electrodes were fabricated by dropcasting a sample as described in the experimental Section 2.5. The Ag/AgCl was the reference electrode and Pt wire the

counter electrode in 1.0 M KOH as the electrolyte. CV and LSV curves of α-Fe_2O_3 were recorded at a potential of 100 Hz and with a scan rate of 100 mV s^{-1}.

3. Results and Discussion

3.1. Characterization

The optical properties of the freshly prepared α-Fe_2O_3 nanoparticles at various pH values were investigated using UV–Vis absorption spectroscopy, and the results are presented in Figure 1. It is clear that the absorption of the colloidal α-Fe_2O_3 begins below 560 nm, indicating that the prepared α-Fe_2O_3 is a visible-light-active photocatalyst. Moreover, the absorption below 560 nm is due to the absorption of shorter wavelengths of the visible region (yellow to ultraviolet photons), and the good transmission of red light which yields the characteristic red colour of hematite.

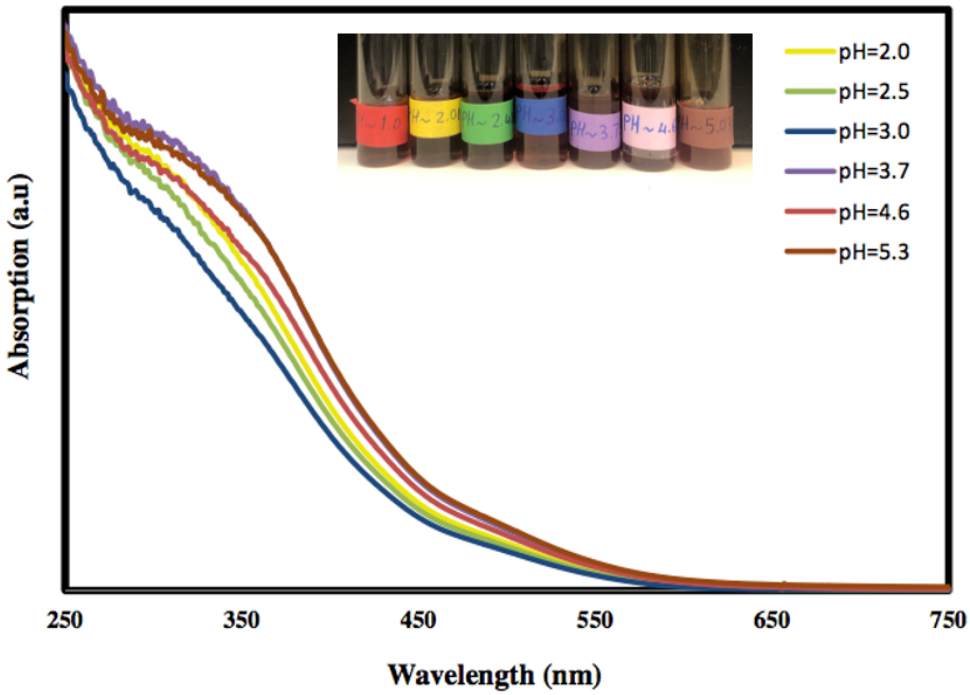

Figure 1. The UV–Visible absorption curves of hematite nanoparticles at different pH values.

FT-IR was used to investigate the successful oxidation of the MWCNTs and preparation of α-Fe_2O_3, as well as the α-Fe_2O_3/O-MWCNTs nanocomposite, and the results are shown in Figure 2. The FTIR spectrum of the pristine MWCNTs showed the characteristic vibration peaks at 1680–1640 cm^{-1} (C=C stretch) and 1500–1400 cm^{-1} (C-C stretch) due to the carbon hexagonal ring of the MWCNT. In contrast, the oxidized MWCNTs (O-MWCNT) spectrum showed a clear and strong absorption peak at 1730 cm^{-1} and a weak peak at 1130 cm^{-1}, which could be attributed to the stretching vibration of C=O corresponding to the stretching vibration of C=O from the carboxylic acid groups (-COOH) and C-O stretching from either a phenol or lactone, which confirmed the successful oxidation of the MWCNTs [31]. The FTIR spectrum of α-Fe_2O_3 showed characteristic Fe-O sharp peaks at 478 and 568 cm^{-1} due to the vibrational mode [32]. Furthermore, the FTIR spectrum of the α-Fe_2O_3/O-MWCNTs nanocomposite showed three new peaks in the range of 1760–1100 cm^{-1}, which appeared after the mixing of α-Fe_2O_3 with O-MWCNT, and band shifting occurred from 600 to 628 cm^{-1}, which indicated that the hematite surface was modified by the oxidized MWCNT. A broad peak at approximately 3500 cm^{-1} for all the investigated samples could be assigned to O-H stretching, due to moisture from the environment, and/or alcoholic, phenolic, or carboxylic groups at the oxidized MWCNTs surface due to oxidation.

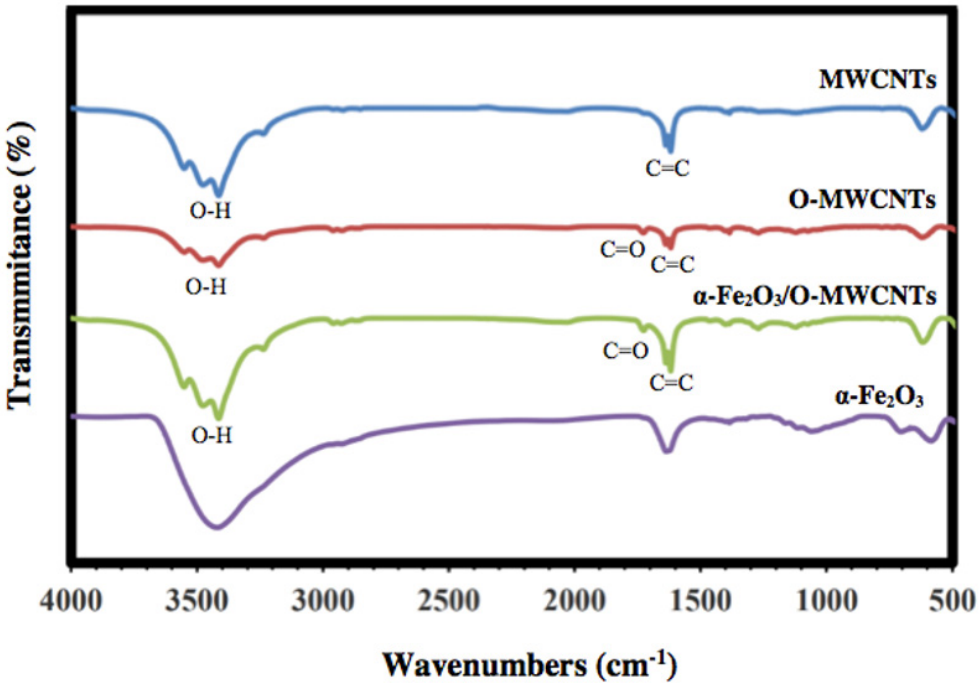

Figure 2. FT-IR spectra of MWCNTs, oxidized MWCNTs, hematite nanoparticles, and hematite/O-MWCNTs nanocomposite.

Figure 3 illustrates the XRD patterns of the prepared α-Fe_2O_3 nanoparticles, O-MWCNTs and the α-Fe_2O_3/O-MWCNTs nanocomposite. According to the XRD, the characteristic peaks of the hexagonal crystal system α-Fe_2O_3 nanoparticles were identified from the diffraction peaks at 2θ = 24.20°, 33.21°, 35.70°, 40.92°, 49.60°, 54.15°, 57.90°, 62.50°, and 64.10°, related to (012), (104), (110), (113), (024), (116), (112), (214), and (300), respectively (JCPDS card no 96-900-9783). Moreover, the sharp peaks of the α-Fe_2O_3 nanoparticles indicate the highly crystalline structure of the hexagonal crystal system, with an average crystallite size of 18.55 nm, as calculated from the Scherer equation. Conversely, O-MWCNTs exhibits two diffraction peaks: one at 26.14° (002 plane) and the other at 44.22° (100 plane), corresponding to graphitic carbon (JCPDS card no 89-8487). Furthermore, the XRD pattern of the α-Fe_2O_3/O-MWCNTs nanocomposite exhibits the characteristic peaks of both the hexagonal crystal system of α-Fe_2O_3 nanoparticles and the oxidized MWCNTs.

The surface binding state and elemental speciation of α-Fe_2O_3 and α-Fe_2O_3/O-MWCNTs composite were analysed by XPS, and the wide-scan XPS survey spectra are presented in Figure 4. The XPS survey spectrum of α-Fe_2O_3 showed sub-peaks at binding energies 711.3, 714.6, and 718.8 eV, as well as their corresponding $Fe2p1_{1/2}$ sub-peaks, corresponding to Fe^{3+} in α-Fe_2O_3 NPs; these sub-peaks are consistent with the oxygen bonds indicated as O1s A, O1s B, and O1s C at binding energies 529.6, 530.7, and 532.3 eV, respectively [33]. In addition, the presence of an insignificant amount of carbon and chlorine within the α-Fe_2O_3 sample may be attributed to the preparation process [33]. The XPS survey spectrum of the α-Fe_2O_3/O-MWCNTs composite and the binding energies for the C 1s and O 1s peaks were observed at approximately 284.5 and 531.0 eV, respectively, corresponding to the carbon and oxygen of the O-MWCNTs [34]. In addition to the sub-peaks of the α-Fe_2O_3, there were no signs of any other impurities in both samples according to the XPS analysis.

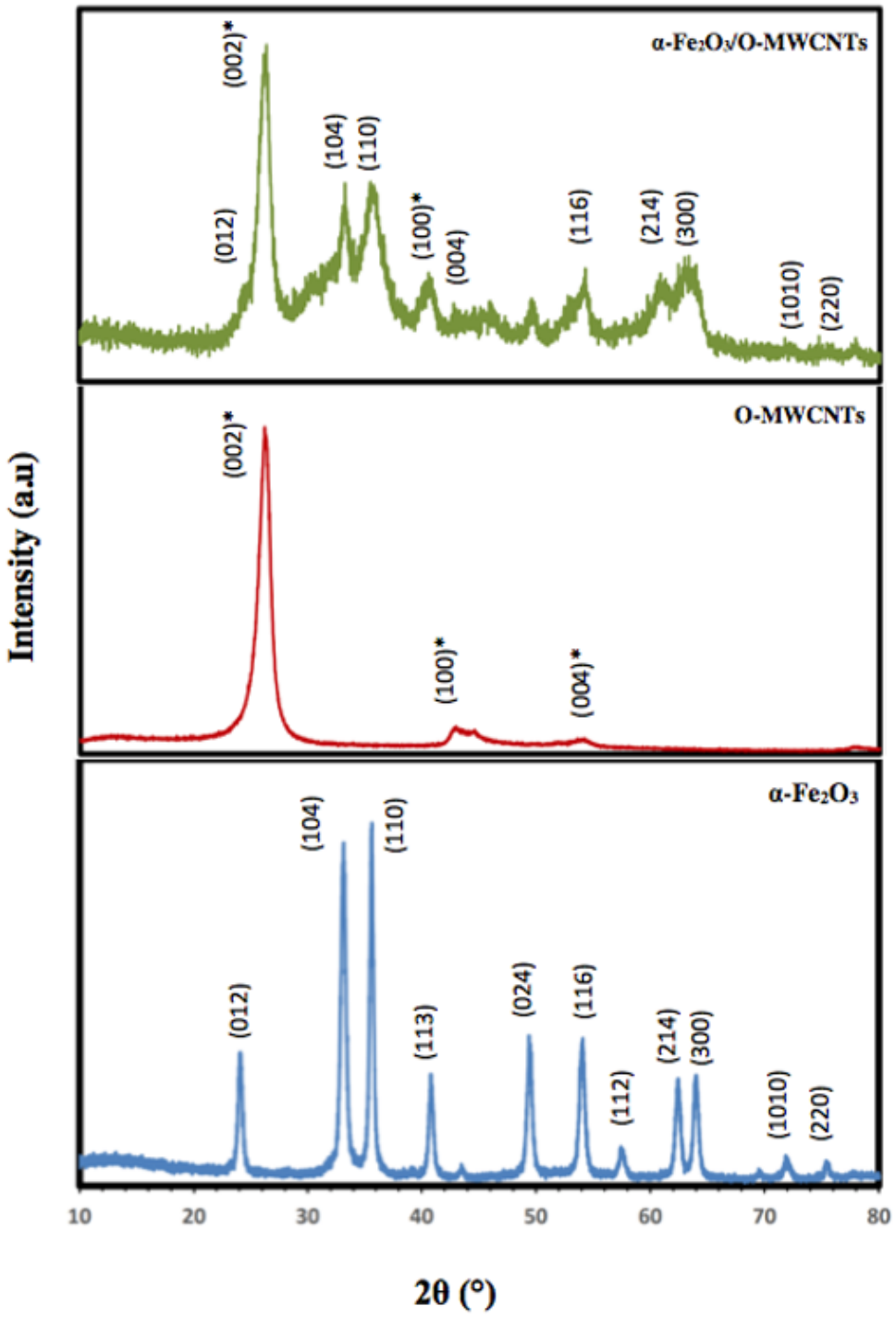

Figure 3. XRD of hematite nanoparticles, oxidized MWCNTs, and hematite/O-MWCNTs nanocomposite (* for the O-MWCNTs).

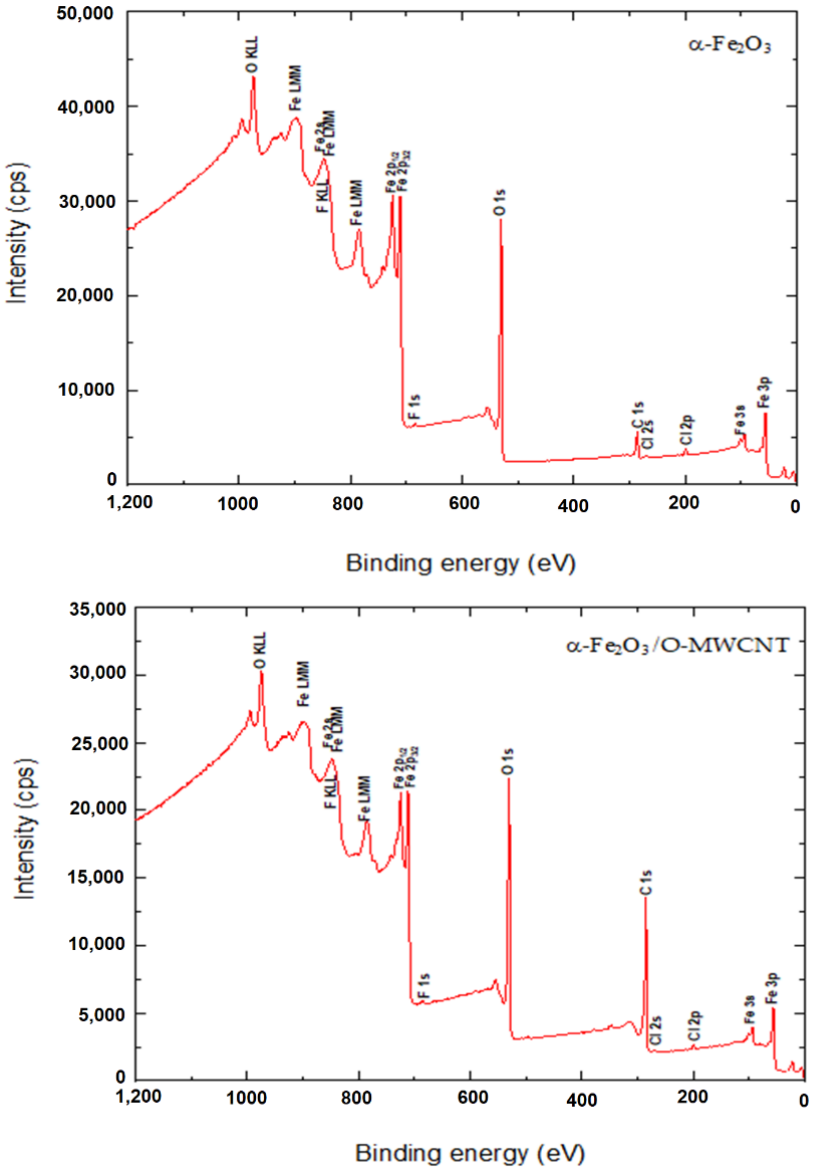

Figure 4. The wide-scan XPS survey spectra α-Fe_2O_3 and α-Fe_2O_3/O-MWCNTs composite.

3.2. Electrochemical Measurements

The prepared α-Fe_2O_3 nanoparticles and its nanocomposite were investigated as an electrode material for supercapacitors, and the electrochemical properties were investigated using cyclic voltammetry (CV) and linear sweep voltammetry (LSV). Figure 5 shows the cyclic voltammograms of the prepared α-Fe_2O_3 in a 1.0 mol/L KOH solution at different pH values in the potential window range of −0.3 to 0.6 V. In general, the CV of the prepared α-Fe_2O_3 nanoparticles exhibited a rectangular shape without redox peaks, indicating the pseudocapacitive behaviour with fast and reversible surface reactions and good capacitive characteristics, which suggests that the α-Fe_2O_3 nanoparticle electrode is an excellent candidate for electrochemical double-layer capacitors. The consistent CV also indicated that the prepared α-Fe_2O_3 nanoparticles exhibited regular capacitive behaviour and excellent cycling stability [35,36].

Moreover, the voltammograms showed an increase in the current density, especially for the cathodic current, with lower pH values which may be due to the reductive dissolution of the α-Fe_2O_3 surface [37]. Moreover, the changes in the anodic current with pH were not significant compared with the cathodic current, and they may result from the oxidation of Fe(III) to Fe(IV) [38].

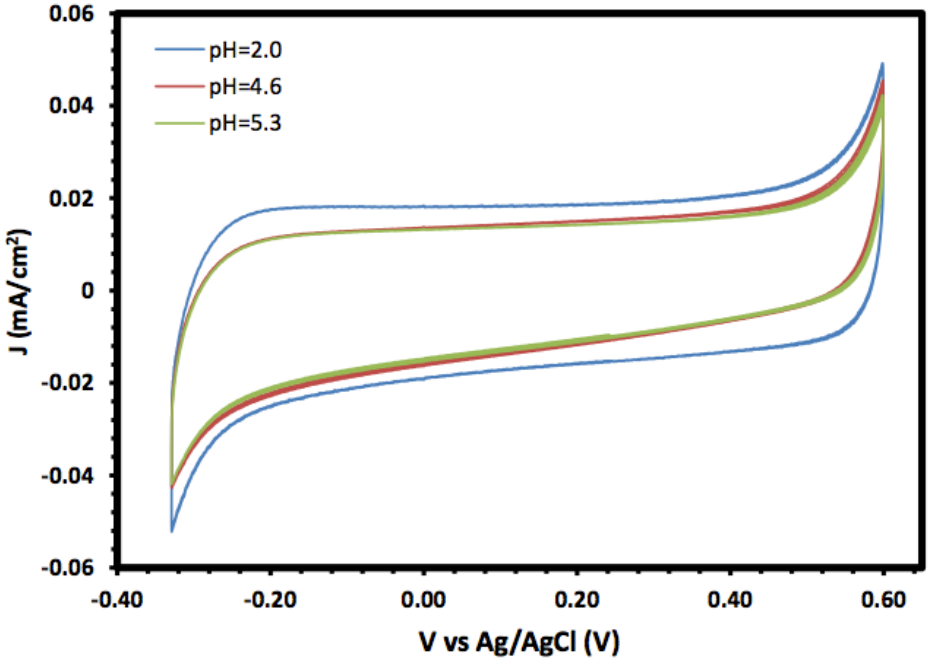

Figure 5. Cyclic voltammetry of α-Fe_2O_3 nanoparticles at different pH values.

Moreover, the electrochemical behaviour of the α-Fe_2O_3 nanoparticles in the absence and presence of O-MWCNTs was studied, and the results are presented in Figure 6. The voltammogram of the O-MWCNTs showed typical double-layer behaviour, and the featureless CV probably resulted from the distribution of the nanotubes, as well as the variations in length, diameter, and helicity of the arrangement of carbon hexagon rings at the working electrode [39]. Conversely, the voltammogram of the α-Fe_2O_3/O-MWCNTs nanocomposite showed the same characteristics as the pseudocapacitive behaviour, which were similar to α-Fe_2O_3, but with higher current density, especially for the cathodic current, which may indicate the enhancement of the reductive dissolution of the α-Fe_2O_3 surface in the presence of the O-MWCNT. The total capacitance is a result of α-Fe_2O_3 pseudocapacitance and EDLC capacitance of the O-MWCNTs [40,41]. Moreover, the variation in the O-MWCNTs within the α-Fe_2O_3/O-MWCNTs nanocomposite had a significant effect, as is presented in Figure 7, as the current density increased when increasing the amount of O-MWCNTs within the α-Fe_2O_3/O-MWCNTs nanocomposite, which may attribute to the enhancement of the specific surface area of the α-Fe_2O_3 electrode upon mixing with more carbon nanotubes.

Figure 8 shows the linear sweep voltammograms (LSV) of O-MWCNT, α-Fe_2O_3 nanoparticles, and α-Fe_2O_3/O-MWCNTs nanocomposite (1.0 mL O-MWCNT) in 1.0 M KOH. It is clear from the figure that the generated current of the α-Fe_2O_3 nanoparticles are greatly enhanced upon the addition of the O-MWCNT, from 5.5×10^{-2} to 9.6×10^{-2} mA/cm^2 for the α-Fe_2O_3 nanoparticles and α-Fe_2O_3/O-MWCNTs nanocomposite, respectively, which is almost 1.74 times higher, indicating the improvement of photoelectrochemical (PEC) performance. This enhancement in PEC performance could be due to the change in the morphology and hydrophilicity of the interface and consequently the faradic current upon the addition of the O-MWCNT, which is presented in Figure 8, as the charging current enhancement greatly depends on the amount of O-MWCNTs loaded.

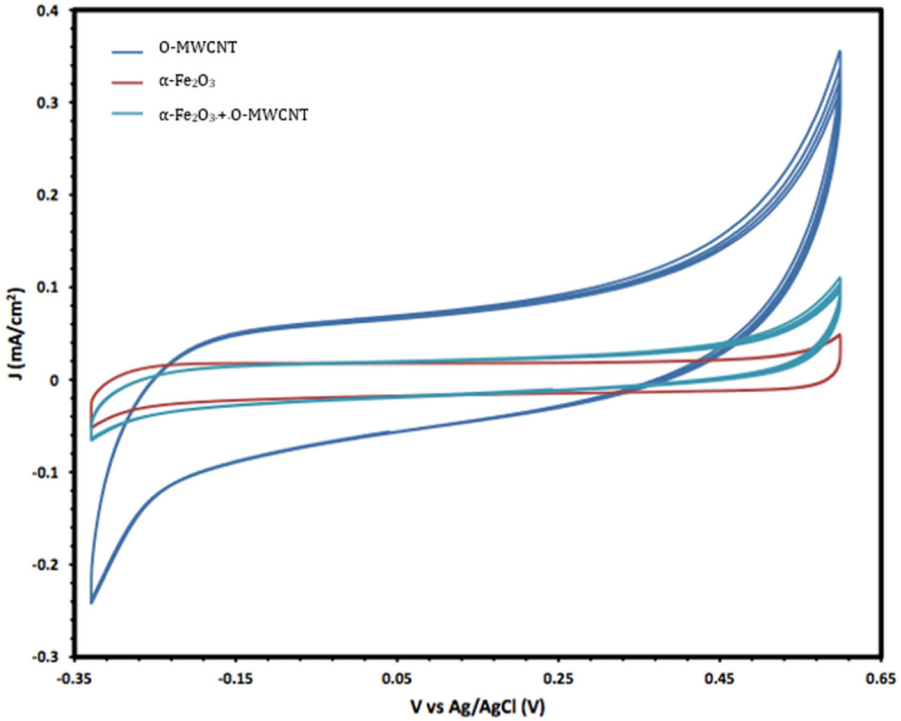

Figure 6. Cyclic voltammetry of O-MWCNT, α-Fe_2O_3 nanoparticles, and α-Fe_2O_3 /O-MWCNTs nanocomposite (1.0 mL O-MWCNT) in 1.0 M KOH.

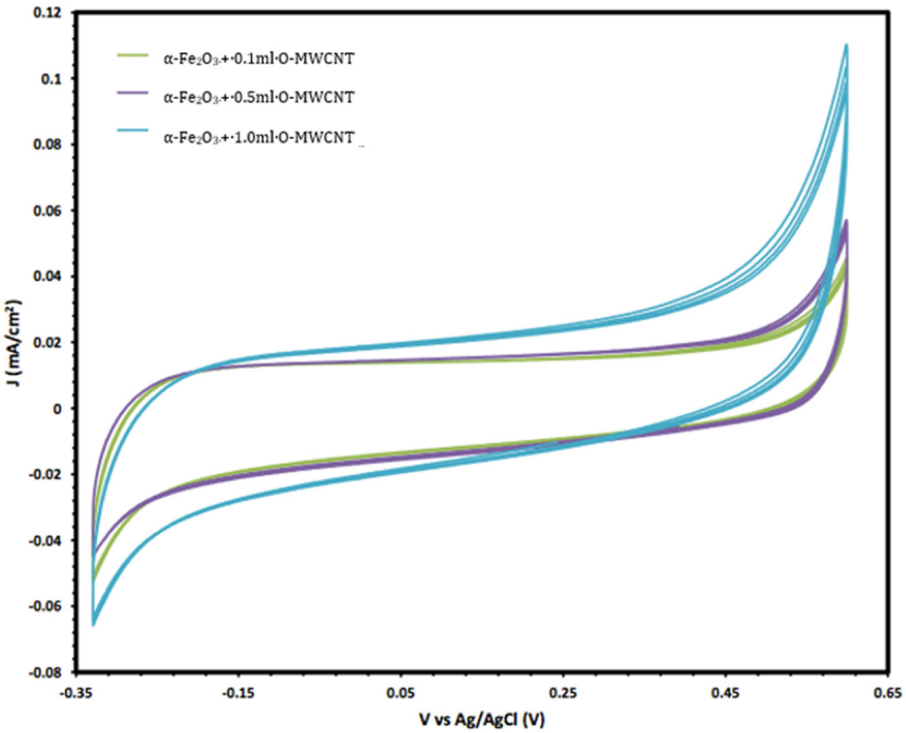

Figure 7. The variation in the cyclic voltammetry of α-Fe_2O_3 /O-MWCNTs nanocomposites with different amounts of O-MWCNTs.

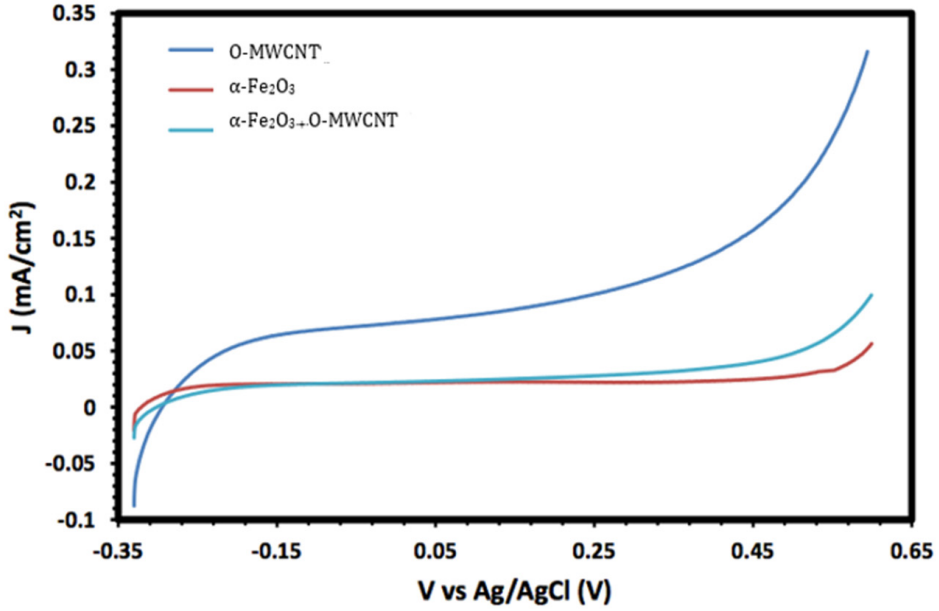

Figure 8. Linear sweep voltammograms (LSV) of O-MWCNT, α-Fe_2O_3 nanoparticles, and α-Fe_2O_3/O-MWCNTs nanocomposite (1.0 mL O-MWCNT) in 1.0 M KOH.

The electrochemical impedance spectroscopy (EIS) of the hematite and its composite with O-MWCNTs was explored, as the EIS measures the opposition of alternating current flow of various frequencies applied to an electrochemical cell, such as a hematite body in contact with an aqueous solution. Figure 9 presents the Nyquist plot of the α -Fe_2O_3, O-MWCNTs, and α -Fe_2O_3/O-MWCNT. The inset in Figure 8 is the suggested equivalent circuit. The fitting results for α -Fe_2O_3, O-MWCNT, and α -Fe_2O_3/O-MWCNTs are summarized in Table 1. Rs is the solution/electrolyte resistance, which includes the contact and charge transfer resistances at the counter electrode/electrolyte (electrode interface) [42]. Rct is the charge-transfer resistance, CPE is the constant phase element, which represents the double-layer capacitance, and Ws is the Warburg impedance, which corresponds to the diffusion of the reactive species at the surface of the electrodes. The contribution of the electrochemical behaviour of the α -Fe_2O_3/O-MWCNTs nanocomposite is identified by the decrease in Rct and the increase in the double-layer capacitance in the presence of the O-MWCNT. The value of the charge-transfer resistance Rct for the a-Fe_2O_3 electrode decreases from 9454.9 Ω to 7236 Ω upon the addition of the O-MWCNTs and the formation of the α -Fe_2O_3/O-MWCNTs composite, while the value of CPE increases from 4.49 mF × cm^{-2} before adding O-MWCNTs to 5.53 mF × cm^{-2} after adding O-MWCNTs. The faster charge transfer is in the α -Fe_2O_3/O-MWCNTs nanocomposite, which may be attributed to an enhancement in the electrochemical behaviour and conductivity of the α -Fe_2O_3/O-MWCNTs nanocomposite.

Table 1. Electrochemical double-layer capacitance, charge transfer resistance and solution resistance of α-Fe_2O_3, MWCNT, and α-Fe_2O_3/MWCNT.

	C_{dl} (mF cm^{-2})	R_{ct} (Ω)	R_s (Ω)
Fe_2O_3	4.49	9454.9	0.51
Fe_2O_3/0.5 mL O-MWCNT	5.53	7236	0.49
MWCNT	9.49E	4656	0.64

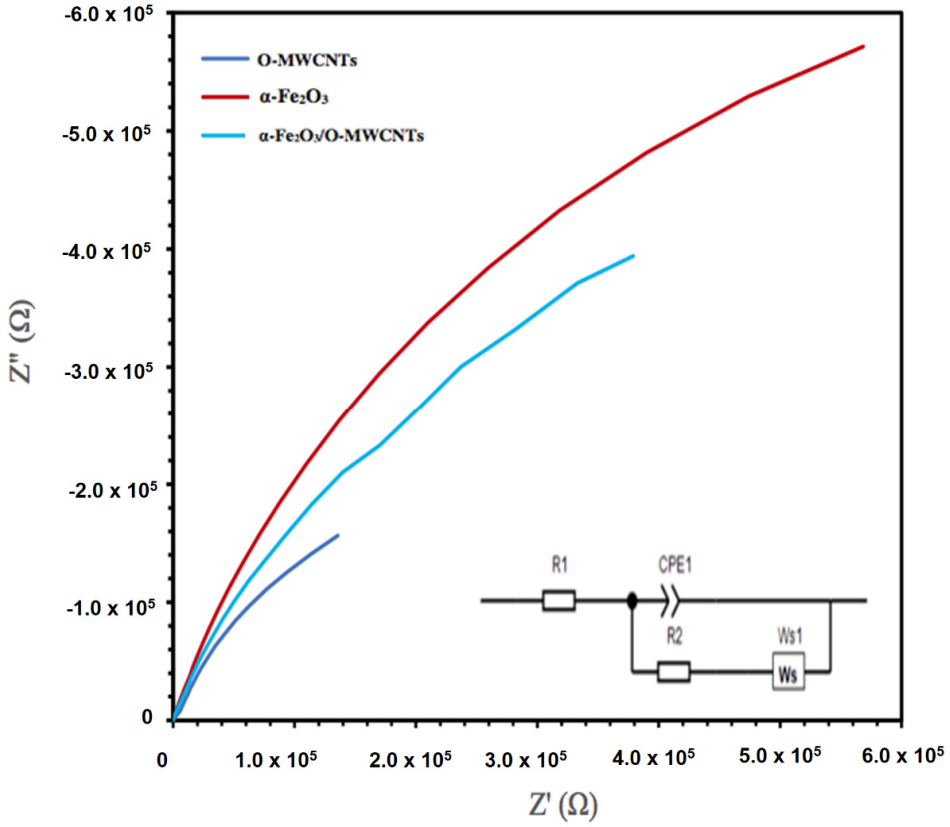

Figure 9. EIS Nyquist plots of O-MWCNT, α-Fe_2O_3 nanoparticles, and α-Fe_2O_3/O-MWCNTs nanocomposite (1.0 mL O-MWCNT) in 1.0 M KOH (inset is the proposed equivalent circuit).

Finally, the chemical stability of the α-Fe_2O_3/O-MWCNTs composite after the electrochemical measurement was explored using the XPS measurement, and the results revealed no change in the XPS survey after the electrochemical measurement (Figure 10), indicating the chemical stability of the α-Fe_2O_3/O-MWCNTs composite.

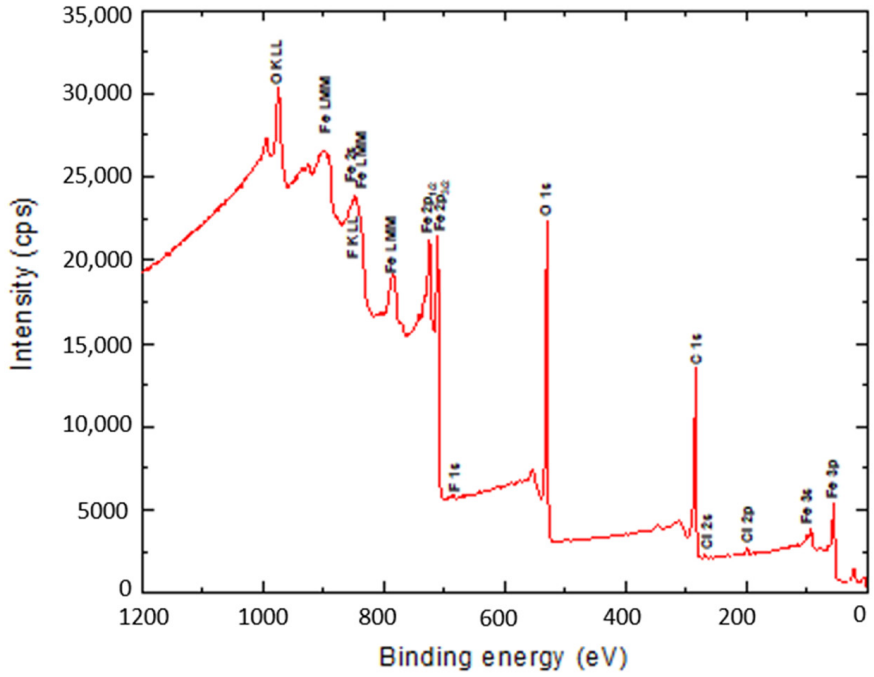

Figure 10. The XPS survey spectrum of the α-Fe_2O_3 and α-Fe_2O_3/O-MWCNTs composite after the electrochemical measurements.

4. Conclusions

The α-Fe_2O_3/O-MWCNTs nanocomposite was successfully prepared using wet chemistry, and it was then characterized chemically and physically using different characterization techniques. UV–Vis absorption spectroscopy showed that the absorption of the colloidal α-Fe_2O_3 begins below 560 nm, indicating that the prepared α-Fe_2O_3 is a visible-light-active photocatalyst, and the FT-IR measurements showed the successful oxidation of the MWCNTs and preparation of the α-Fe_2O_3, as well as the α-Fe_2O_3/O-MWCNTs nanocomposite through the presence of their characteristic vibration peaks, whereas the XRD measurements showed the characteristic diffraction peaks of graphitic carbon nanotubes. The electrochemical behaviour of the α-Fe_2O_3/O-MWCNTs nanocomposite was investigated using cyclic voltammetry (CV), linear sweep voltammetry (LSV), and electrochemical impedance spectroscopy, and the results revealed that modification of the α-Fe_2O_3 nanoparticles with O-MWCNTs greatly enhanced electrochemical performance, conductivity and capacitive behaviour, as well as cycling stability.

Author Contributions: Data curation, H.M.B. and M.A.S., methodology; M.A.S. and L.M.A.; investigation, H.M.B. and M.A.S.; validation, M.A.S. and L.M.A.; supervision, M.A.S. and L.M.A.; formal analysis, M.A.S., M.J. and R.H.A.-D.; visualization, H.M.B., L.M.A.; resources, M.A.S., M.J.; writing—original draft, H.M.B., M.A.S.; writing—review and editing, M.A.S. and L.M.A. All authors have read and agreed to the published version of the manuscript.

Funding: This research received no external funding.

Institutional Review Board Statement: Not applicable.

Informed Consent Statement: Not applicable.

Data Availability Statement: Not applicable.

Conflicts of Interest: The authors declare no conflict of interest.

Sample Availability: Samples of the compounds are available from the authors.

References

1. Nazri, G.-A.; Pis-toia, G. *Lithium Batteries: Science and Technology*; Kluwer Academic: New York, NY, USA, 2003.
2. Poizot, P.; Laruelle, S.; Grugeon, S.; Dupont, L.; Tarascon, J.-M. Nano-sized transition-metal oxides as negative-electrode materials for lithium-ion batteries. *Nature* **2000**, *407*, 496–499. [CrossRef] [PubMed]
3. Arico, A.S.; Bruce, P.G.; Scrosati, B.; Tarascon, J.-M.; Schalkwijk, W.V. Nanostructured materials for advanced energy conversion and storage devices. *Nat. Mater.* **2005**, *4*, 366. [CrossRef] [PubMed]
4. Li, Q.; Li, H.; Xia, Q.; Hu, Z.; Zhu, Y.; Yan, S.; Ge, C.; Zhang, Q.; Wang, X.; Shang, X.; et al. Extra storage capacity in transition metal oxide lithium-ion batteries revealed by in situ magnetometry. *Nat. Mater.* **2021**, *20*, 76–83. [CrossRef] [PubMed]
5. Sivula, K.; Formal, F.L.; Grätzel, M. Solar Water Splitting: Progress Using Hematite (α-Fe_2O_3) Photoelectrodes. *ChemSusChem* **2011**, *4*, 432–449. [CrossRef] [PubMed]
6. Sharma, B.; Sharma, A. Enhanced surface dynamics and magnetic switching of α-Fe_2O_3 films prepared by laser assisted chemical vapor deposition. *Appl. Surf. Sci.* **2021**, *567*, 150724. [CrossRef]
7. Long, N.V.; Teranishi, T.; Yang, Y.; Thi, C.M.; Cao, Y.; Nogami, M. Iron oxide nanoparticles for next generation gas sensors. *Int. J. Metall. Mater. Eng.* **2015**, *1*, 119. [CrossRef]
8. Vangijzegem, T.; Stanicki, D.; Laurent, S. Magnetic iron oxide nanoparticles for drug delivery. applications and characteristics. *Expert Opin. Drug Deliv.* **2019**, *16*, 69–78. [CrossRef]
9. Lunin, A.V.; Lizunova, A.A.; Mochalova, E.N.; Yakovtseva, M.N.; Cherkasov, V.R.; Nikitin, M.P.; Kolychev, E.L. Hematite Nanoparticles from Unexpected Reaction of Ferrihydrite with Concentrated Acids for Biomedical Applications. *Molecules* **2020**, *25*, 1984. [CrossRef]
10. Wu, C.; Yin, P.; Zhu, X.; OuYang, C.; Xie, Y. Synthesis of Hematite (α-Fe_2O_3) Nanorods: Diameter-Size and Shape Effects on Their Applications in Magnetism, Lithium Ion Battery, and Gas Sensors. *J. Phys. Chem. B* **2006**, *110*, 17806–17812. [CrossRef]
11. Xu, L.; Tian, Y.; Liu, T.; Li, H.; Qiu, J.; Li, S.; Li, H.; Yuan, S.; Zhang, S. α-Fe_2O_3 nanoplates with superior electrochemical performance for lithium-ion batteries. *Green Energy Environ.* **2018**, *3*, 156–162. [CrossRef]
12. Lin, Y.-M.; Abel, P.R.; Heller, A.; Mullins, C.B. α-Fe_2O_3 Nanorods as Anode Material for Lithium Ion Batteries. *J. Phys. Chem. Lett.* **2011**, *2*, 2885–2891.
13. Yao, J.; Yang, Y.; Li, Y.; Jiang, J.; Xiao, S.; Yang, J. Interconnected α-Fe_2O_3 nanoparticles prepared from leaching liquor of tin ore tailings as anode materials for lithium-ion batteries. *J. Alloys Compd.* **2021**, *855*, 157288. [CrossRef]

14. Muhajir, M.; Puspitasari, P.; Razak, J.A. Synthesis and applications of Hematite α-Fe_2O_3: A Review. *J. Mech. Eng. Sci. Technol.* **2020**, *3*, 51–58.
15. Iandolo, B.; Wickman, B.; Zorić, I.; Hellman, A. The rise of hematite: Origin and strategies to reduce the high onset potential for the oxygen evolution reaction: Review Article. *J. Mater. Chem. A* **2015**, *3*, 16896–16912.
16. Dalle Carbonare, N.; Boaretto, R.; Caramori, S.; Argazzi, R.; Dal Colle, M.; Pasquini, L.; Bertoncello, R.; Marelli, M.; Evangelisti, C.; Bignozzi, C.A. Photoelectrochemical Behavior of Electrophoretically Deposited Hematite Thin Films Modified with Ti(IV). *Molecules* **2016**, *21*, 942. [CrossRef] [PubMed]
17. Krysa, J.; Zlamal, M.; Kment, S.; Brunclikova, M.; Hubicka, Z. TiO_2 and Fe_2O_3 Films for Photoelectrochemical Water Splitting. *Molecules* **2015**, *20*, 1046–1058. [CrossRef] [PubMed]
18. Chen, D.; Liu, Z. Dual-Axial Gradient Doping (Zr and Sn) on Hematite for Promoting Charge Separation in Photoelectrochemical Water Splitting. *ChemSusChem* **2018**, *11*, 3438–3448. [CrossRef]
19. Zhang, H.; Li, D.; Byun, W.J.; Wang, X.; Shin, T.J.; Jeong, H.Y.; Han, H.; Li, C.; Lee, J.S. Gradient tantalum-doped hematite homojunction photoanode improves both photocurrents and turn-on voltage for solar water splitting. *Nat. Commun.* **2020**, *11*, 4622. [CrossRef]
20. Ahn, H.-J.; Yoon, K.-Y.; Kwak, M.-J.; Park, J.; Jang, J.-H. Boron Doping of Metal-Doped Hematite for Reduced Surface Recombination in Water Splitting. *ACS Catal.* **2018**, *8*, 11932–11939. [CrossRef]
21. Wang, X.; Gao, W.; Zhao, Z.; Zhao, L.; Claverie, J.P.; Zhang, X.; Wang, J.; Liu, H.; Sanga, Y. Efficient photo-electrochemical water splitting based on hematite nanorods doped with phosphorus. *Appl. Catal. B Environ.* **2019**, *248*, 388–393.
22. Rauf, A.; Adil, M.; Mian, S.A.; Rahman, G.; Ahmed, E.; Ud Din, Z.M.; Qun, W. Tuning the optoelectronic properties of hematite with rhodium doping for photoelectrochemical water splitting using density functional theory approach. *Sci. Rep.* **2021**, *11*, 2045–2322. [CrossRef] [PubMed]
23. Subramanian, A.; Gracia-Espino, E.; Annamalai, A.; Lee, H.H.; Lee, S.Y.; Choi, S.H.; Jang, J.S. Effect of tetravalent dopants on hematite nanostructure for enhanced photoelectrochemical water splitting. *Appl. Surf. Sci.* **2018**, *427*, 1203–1212. [CrossRef]
24. Hu, X.; Huang, J.; Zhao, F.; Yi, P.; He, B.; Wang, Y.; Chen, T.; Chen, Y.; Li, Z.; Liu, X. Photothermal effect of carbon quantum dots enhanced photoelectrochemical water splitting of hematite photoanodes. *J. Mater. Chem. A* **2020**, *8*, 14915–14920. [CrossRef]
25. Liu, C.; Fu, Y.; Xia, Y.; Zhu, C.; Hu, L.; Zhang, K.; Wu, H.; Huang, H.; Liu, Y.; Xie, T.; et al. Cascaded photo-potential in a carbon dot-hematite system driving overall water splitting under visible light. *Nanoscale* **2018**, *10*, 2454–2460. [CrossRef] [PubMed]
26. Chu, D.; Li, K.; Liu, A.; Huang, j.; Zhang, C.; Yang, P.; Du, Y.; Lu, C. Zn-doped hematite modified by graphene-like WS2: A p-type semiconductor hybrid photocathode for water splitting to produce hydrogen. *Int. J. Hydrogen Energy* **2018**, *43*, 7307–7316. [CrossRef]
27. Cardona, M.P.; Li, M.; McCall, J.; Wang, D.; Li, Y.; Yang, C. The role of graphene as an overlayer on nanostructured hematite photoanodes for improved solar water oxidation. *Mater. Today Energy* **2018**, *8*, 8–14. [CrossRef]
28. Poaty, L.T.; M'Passi-Mabiala, B.; Gebauer, R. The oxygen evolution reaction in hematite—Carbon nanotube composites: Insights from density functional theory. *Comput. Condens. Matter* **2020**, *24*, 2143–2352. [CrossRef]
29. Niyitanga, T.; Kim, H. Hematite-nickel oxide/carbon nanotube composite catalyst for oxygen evolution reaction. *Mater. Chem. Phys.* **2022**, *275*, 125266. [CrossRef]
30. Faust, B.C.; Hoffmann, M.R.; Bahnemann, D.W. Photocatalytic oxidation of sulfur-dioxide in aqueous suspensions of alpha-Fe_2O_3. *J. Phys. Chem.* **1989**, *93*, 6371–6381. [CrossRef]
31. Abdel Salam, M. Effect of oxidation treatment of multi-walled carbon nanotubes on the adsorption of pentachlorophenol from aqueous solution: Kinetics study. *Arab. J. Chem.* **2012**, *5*, 291–296. [CrossRef]
32. Rufus, A.; Sreeju, N.; Philip, D. Synthesis of biogenic hematite (α-Fe_2O_3) nanoparticles for antibacterial and nanofuid applications. *RSC Adv.* **2016**, *6*, 94206–94217. [CrossRef]
33. Farhanian, D.; De Crescenzo, G.; Tavares, J.R. Large-Scale Encapsulation of Magnetic Iron Oxide Nanoparticles via Syngas Photo-Initiated Chemical Vapor Deposition. *Sci. Rep.* **2018**, *8*, 12223. [CrossRef] [PubMed]
34. Fan, Y.; Su, F.; Li, K.; Ke, C.; Yan, Y. Carbon nanotube filled with magnetic iron oxide and modified with polyamidoamine dendrimers for immobilizing lipase toward application in biodiesel production. *Sci. Rep.* **2017**, *7*, 45643. [CrossRef] [PubMed]
35. Jurewicz, K.; Vix-Guterl, C.; Frackowiak, E.; Saadallah, S.; Reda, M.; Parmentier, J.; Patarin, J.; Beguin, F. Capacitance properties of ordered porous carbon materials prepared by a templating procedure. *Phys. Chem. Solids* **2004**, *65*, 287–293. [CrossRef]
36. Barik, R.; Jena, B.K.; Dash, A.; Mohapatra, M. In situ synthesis of flowery-shaped α-FeOOH/Fe_2O_3 nanoparticles and their phase dependent supercapacitive behaviour. *RSC Adv.* **2014**, *4*, 18827–18834. [CrossRef]
37. Shimizu, K.; Lasia, A.; Boily, J.-F. Electrochemical Impedance Study of the Hematite/Water Interface. *Langmuir* **2012**, *28*, 7914–7920. [CrossRef]
38. Wijayantha, U.K.G.; Saremi-Yarahmadi, S.; Peter, L.M. Kinetics of oxygen evolution at α-Fe_2O_3 photoanodes: A study by photoelectrochemical impedance spectroscopy. *Chem. Phys.* **2011**, *13*, 5264–5270. [CrossRef]
39. Chen, J.H.; Li, W.Z.; Wang, D.Z.; Yang, S.X.; Wen, J.G.; Ren, Z.F. Electrochemical characterization of carbon nanotubes as electrode in electrochemical double-layer capacitors. *Carbon* **2002**, *40*, 1193–1197. [CrossRef]
40. Signorelli, R.; Ku, D.C.; Kassakian, J.G.; Schindall, J.E. Electrochemical Double-Layer Capacitors Using Carbon Nanotube Electrode Structures. *Proc. IEEE* **2009**, *97*, 1837–1847. [CrossRef]

41. Dawoud, H.D.; Al Tahtamouni1, T.; Bensalah, N. Sputtered manganese oxide thin film on carbon nanotubes sheet as a flexible and binder-free electrode for supercapacitors. *Int. J. Energy Res.* **2019**, *43*, 1245–1254. [CrossRef]
42. Bessekhouad, Y.; Brahimi, R.; Hamdini, F.; Trari, H.M. Cu2S/TiO2 heterojunction applied to visible light Orange II degradation. *J. Photochem. Photobiol. A* **2012**, *248*, 15–23. [CrossRef]